

Anion and Cation Migration at 2D/3D Halide Perovskite Interfaces

Raphael F. Moral, Carlo A. R. Perini,* Tim Kodalle, Ahyoung Kim, Finn Babbe, Nao Harada, Javid Hajhemati, Philip Schulz, Naomi S. Ginsberg, Shaul Aloni, Craig P. Schwartz, Juan-Pablo Correa-Baena,* and Carolin M. Sutter-Fella*



Cite This: *ACS Energy Lett.* 2024, 9, 2703–2716



Read Online

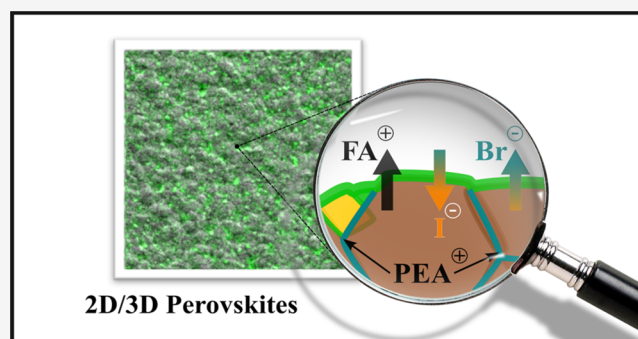
ACCESS |

Metrics & More

Article Recommendations

Supporting Information

ABSTRACT: This study explores the ionic dynamics in 2D/3D perovskite solar cells, which are known for their improved efficiency and stability. The focus is on the impact of halide choice in 3D perovskites treated with phenethylammonium halide salts (PEAX, X = Br and I). Our findings reveal that light and heat drive ionic migration in these structures, with PEA⁺ species diffusing into the 3D film in PEABr-treated samples. Mixed-halide 3D perovskites show halide interdiffusion, with bromine migrating to the surface and iodine diffusing into the film. Cathodoluminescence microscopy reveals localized 2D phases on the 3D perovskite, which become more evenly distributed after thermal treatment. Both PEAX salts enhance the performance of photovoltaic devices. This improvement is attributed to the passivation capabilities of the salts themselves and their respective Ruddlesden–Popper (RP) phases. Annealed PEAI-treated devices show a better balance between efficiency and statistical distribution of photovoltaic parameters.



Perovskite-based solar cells (PSCs) with general structure ABX₃, where A = a monovalent cation such as Cs⁺, formamidinium (FA⁺), and methylammonium (MA⁺); B = Sn²⁺ or Pb²⁺; and X = Cl⁻, Br⁻, and I⁻, have seen rapid development in terms of power conversion efficiency (PCE) but are lacking device stability.^{1–4} A common way to improve the ambient stability of devices is the passivation of the active 3D perovskite layer with more stable two-dimensional (2D) perovskites.^{1,5} By simply coating the 3D perovskite film with a solution of an alkyl or arylammonium cation salt, a 2D or quasi-2D layered perovskite phase is formed on the surface of the film.^{6,7} The chemical composition of such layered materials is L₂A_{n-1}B_nX_{3n+1}, where L is the organic cation and n is the number of inorganic layers of [BX₆]⁴⁻ octahedra (slabs).⁸ In the cases of phenethylammonium iodide or bromide (PEAX) salts, the formed layered perovskites are known as Ruddlesden–Popper (RP) phases. Currently, RP phases are used in most highly efficient 2D/3D PSCs.^{5,9–12} Because the molecular backbones of bulky L-site organic cations are mostly hydrophobic, the ambient stability of the films toward humidity improves.¹³

Although the coating of 3D perovskites with RP phases improves the efficiency and room-temperature stability of solar cell devices, several studies have shown that the 2D/3D

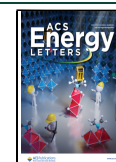
interface transforms under exposure to light and/or prolonged heat.^{14,15} This contrast is due to the dynamic nature of the 2D/3D perovskite interface. For instance, Sutanto and colleagues showed that prolonged thermal annealing (50 °C for more than 2 h) of 2D/3D perovskites based on PEAI and 2-thiophene methylammonium iodide (TMAI) on (CsMAFA)-Pb(I,Br)₃ caused constant changes in the structure of the RP phases: in general they degraded over time, and more n ≥ 2 RP phases formed (n ≤ 2 for PEAI and n ≥ 2 for TMAI).^{6,15} In this case, the device performance decreased slightly. In contrast, Perini and co-workers showed a faster degradation of the 2D/3D PSCs (based on (CsMAFA)Pb(I,Br)₃) treated with PEAI and octylammonium bromide (OABr), compared to the untreated devices; the stability test was performed under inert atmosphere, 1 Sun irradiance, and 55 °C for 1000 h.¹⁴ The authors correlated this lower stability with changes caused

Received: March 12, 2024

Revised: April 24, 2024

Accepted: May 8, 2024

Published: May 14, 2024



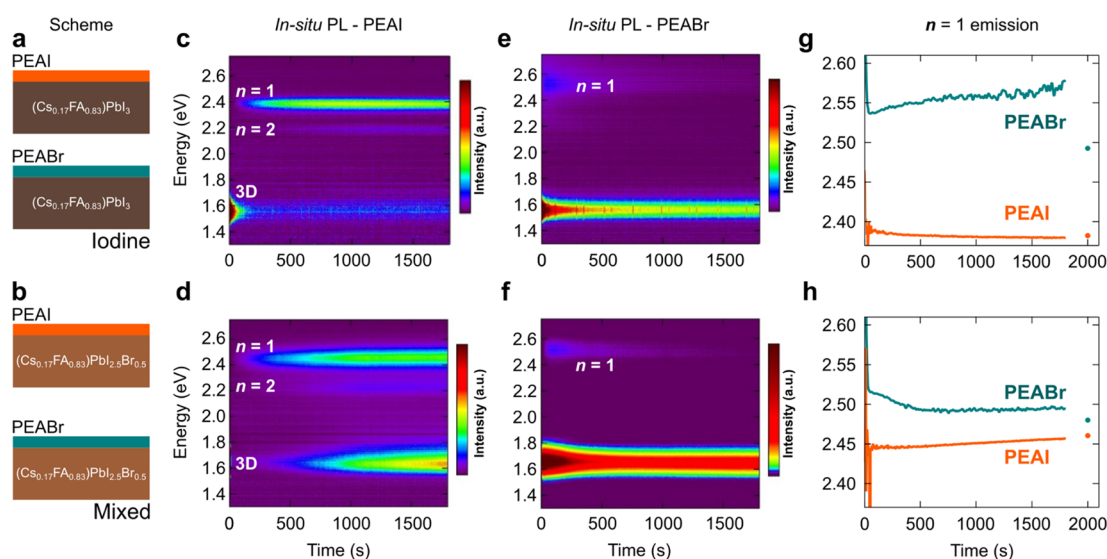


Figure 1. (a, b) Scheme showing the four combinations of 2D/3D perovskites investigated in this work (left side). *Iodine* samples are at the top row and *mixed* samples at the bottom row. *In situ* PL color maps taken during annealing for (c, d) PEAI-treated and (e, f) PEABr-treated samples. Gaussian fit to the $n = 1$ RP phase emissions of (g) *iodine*-PEAI (orange) and *iodine*-PEABr (dark cyan) and (h) *mixed*-PEAI (orange) and *mixed*-PEABr (dark cyan). Separate dots in panels g and h are PL spectra collected during annealing at a fresh spot.

by ionic migration at the 2D/3D interface during thermal annealing and device operation, including higher halide heterogeneity on the PEAI-treated surfaces. Furthermore, some reports have shown that the type of halide used in 2D-forming salts can significantly affect the interface between 2D and 3D materials and therefore the performance of the device. One study by Liu *et al.* looked at how neo-pentylammonium halides (neoPAX) affect $\text{FA}_{1-x}\text{MA}_x\text{PbI}_3$ perovskites.¹⁶ They discovered that the presence of Cl^- anions in neoPACl greatly affects the crystallization of the RP phases, leading to a mix of $n = 1$ and $n = 2$ phases. The authors attributed this difference to an interplay between electronegativity and coordination ability of halide anions. The use of neoPACl led to improved device performance due to effective chlorine passivation and the creation of an $n = 2$ RP phase, which enhances charge transfer at the 2D/3D interface. On the other hand, Sutanto *et al.* reported that TMA^+ cations tend to form $n = 2$ RP phases regardless of the halide used, highlighting the influence of the cations' chemical structure on the formation of RP phases.¹⁷ They demonstrated that treating $[(\text{FAPbI}_3)_{0.87}(\text{MAPbBr}_3)_{0.13}]_{0.92}(\text{CsPbI}_3)_{0.08}$ perovskites with TMABr resulted in favorable band bending at the interface, better charge transport, and reduced voltage loss, thus improving device performance compared to treatments with TMAI and TMACl.

The complexity of 2D/3D interfaces in halide perovskite solar cells and the interdependence on the nature of the L-site cation, halide selection, and 3D perovskite composition leave many unanswered questions. Here we sought to answer the question “how does the halide choice impact the 2D/3D interface formation, ion migration, and device performance?” We evaluate the formation of 2D layered perovskites using PEAI and PEABr salts on top of iodine-only and mixed-halide 3D perovskites ($\text{Cs}_{0.17}\text{FA}_{0.83}\text{PbI}_3$ and $\text{Cs}_{0.17}\text{FA}_{0.83}\text{PbI}_{2.5}\text{Br}_{0.5}$, respectively). The resulting 2D/3D interfaces were investigated before, during, and after prolonged annealing at 65 °C for 30 min. A prolonged annealing is selected on purpose, to drive interface dynamics that could occur during solar cell operation where module temperatures can easily reach 65

°C.¹⁴ *In situ* photoluminescence (PL) measurements during annealing showed mostly iodine-rich $\text{PEA}_2\text{PbI}_{4-x}\text{Br}_x$ 2D perovskite with both PEAX salts, although treatment with PEABr led to a higher Br content in the RP phases. X-ray photoelectron spectroscopy (XPS) showed clear ionic migration of PEA^+ and FA^+ cations and both halide species (Br^- and I^-). Notably, the diffusion of PEA^+ cations is exclusive to PEABr-treated samples. FA^+ cations migrate to the surface of the 2D films upon annealing, causing the formation of $n = 2$ RP phase. In 3D mixed-halide perovskites with PEABr and PEAI treatment, we found an interdiffusion between iodine and bromine anions, with Br^- moving to the surface and I^- diffusing into the film. Finally, we summarized the work with an assessment of solar cell devices based on these 2D/3D films. The best performance and reproducibility were achieved with annealed PEAI-treated devices for both pure-iodine and mixed-halide 3D perovskites.

3D perovskite films, composed of $\text{Cs}_{0.17}\text{FA}_{0.83}\text{PbI}_3$ and $\text{Cs}_{0.17}\text{FA}_{0.83}\text{PbI}_{2.5}\text{Br}_{0.5}$, were prepared, and details of their preparation can be found in **Materials and Methods**. We will refer to the pure-iodine 3D perovskite as “*iodine*” and the mixed-halide 3D perovskite as “*mixed*” (scheme of Figure 1a,b). These films were coated with solutions of 2D-forming PEAX salts ($X = \text{I}$ or Br) in isopropanol (IPA). Nonannealed samples are labeled with 0, while the annealed samples have the number 30 to indicate the 30 min annealing at 65 °C. Previous results with PEACl treatment revealed poorer performance of devices, and we discontinued this salt in this work. The effect of chlorine and PEACl treatments can be found elsewhere.^{16,18}

First, *in situ* PL ($\lambda_{\text{exc}} = 405 \text{ nm}$, 3.06 eV) measurements during annealing at 65 °C were performed to track the emission evolution of the RP phases and 3D perovskites (scheme in Figure S1).^{7,19} Around 1.55 and 1.65 eV, there is the emission of the bulk 3D *iodine* and *mixed* perovskites, respectively (Figure 1c,d and Figure S2a,b). At energies above 2 eV, the emission of the RP phases is observed. According to the literature, $n = 1$ and $n = 2$ emission maxima for $\text{PEA}_2\text{A}_{n-1}\text{Pb}_{n-1}\text{I}_{3n+1}$ are at approximately 2.4 eV²⁰ and 2.2

eV,^{6,7} respectively, and for the bromine analogues at 3.0 eV²¹ and 2.8 eV.²² The *iodine*-PEAI sample presents peaks for both $n = 1$ and $n = 2$ RP phases with emission peak positions in agreement with the literature (Figure 1c). The *mixed*-PEAI sample shows the same RP phases with blue-shifted PL peaks (Figure 1d), a clear indication of halide interdiffusion, with bromine incorporation into the surficial RP phases. In both samples, the PL signal of the RP phases becomes visible in the false color maps after ~ 120 s of thermal annealing for $n = 1$ phase and after 500 s for $n = 2$ phase. This delay suggests that most of the RP phases form upon annealing, rather than during spin-coating, in agreement with a recent report.⁷ For the *iodine*-PEABr and *mixed*-PEABr samples, the PL signal for the $n = 1$ RP phase is visible from the beginning of the annealing but suffers a drastic intensity quench before 500 s (Figure 1e,f). The $n = 2$ RP phase is not visible in the *in situ* PL of both samples. Also, the emission peaks from the $n = 1$ RP phases are blue-shifted compared to the *iodine*-PEAI analogue. This blue shift is due to the halide diffusion at the interface, leading to the formation of mixed-halide RP phases with wider bandgap.^{23–25} We disregard the presence of pure-bromine RP-phases for reasons that will be clearer further below.

Next, hyperspectral PL (HyPL) at $\lambda_{\text{exc}} = 405$ nm was carried out, and the hyperspectral images (Figure S3) were integrated to generate the HyPL spectra for each sample (Figure S4). With the integrated HyPL, we obtain an averaged emission profile from the whole sample. All samples show highly homogeneous PL, with less than 1% intensity variation and less than 1 nm peak position variation for both 3D perovskites (Figure S3). Most spectra show three emission peaks stemming from the bulk 3D perovskite and the two RP phases. The *iodine*-PEAI and -PEABr samples present peaks for both $n = 1$ and $n = 2$ RP phases with emission peak positions in agreement with *in situ* PL (Figure S4a). The relative intensity of the $n = 1$ phase increases after annealing for *iodine*-PEAI. In the *mixed*-PEAI sample, the HyPL intensity of the RP phases is low, and it is not visible for *mixed*-PEABr (Figure S4b). HyPL also shows blue-shifted RP emission peaks, compared to the *iodine*-PEAI. While the $n = 2$ RP phase is not detectable by *in situ* PL for the *iodine*-PEABr sample (Figure 1c), it is visible in the HyPL data of Figure S4a. This is likely due to HyPL's excitation power being ten times higher than what was used for *in situ* PL measurements (see Materials and Methods). It is noted that any emission above 3.06 eV cannot be accessed with the laser excitation energy used for HyPL and *in situ* PL measurements. In addition, HyPL was performed in an ambient atmosphere, in stark contrast to *in situ* PL, which was performed on fresh samples in the glovebox (see extended note on the effect of humidity and oxygen on the PL signal in the Supporting Information).

To gain more insights into the dynamics of the 2D/3D interfaces and laser illumination effects, we extracted the PL peak positions from the *in situ* PL data using Gaussian peak fitting of the $n = 1$ RP phases and 3D perovskites (Figure 1g,h and Figure S2c,d). We observe laser-induced degradation and laser-induced ionic migration in different proportions, depending on the sample's composition. It is well-reported that 3D metal halide perovskites with diverse compositions may suffer from several irradiation effects such as halide segregation^{26–30} and photochemical reactions,^{31,32} which can increase halide vacancies and the density of defects.³³ Note that these effects can be enhanced or accelerated by the elevated temperature

during annealing. Examples of laser effects are given in the Supplementary Text and ref 7.

Looking at the peak positions of the $n = 1$ RP phases, the *iodine*- and *mixed*-PEAI samples show emissions from PEA_2PbI_4 , at approximately 2.38 eV, and from $\text{PEA}_2\text{PbI}_{4-x}\text{Br}_x$, at 2.46 eV, respectively (Figure 1g,h, orange curves). The 0.08 eV increase in the PL peak of the *mixed*-PEAI sample confirms that some bromine from the *mixed* 3D perovskite diffuses into the RP phases (Figure 1g). For both *iodine*- and *mixed*-PEAI samples, we observe a nearly constant PL peak position of the RP phases, even on a fresh sample spot during annealing (Figure 1g,h, orange dots); this indicates no significant laser effect during measurement, which aligns with the steady PL of the RP phases observed in the color maps of Figure 1c,d. The PL position of the RP phases of the *iodine*- and *mixed*-PEABr samples are depicted in Figure 1g,h, cyan curves, at approximately 2.55 and 2.50 eV, respectively. The positions of their PL peaks also evidence the formation of mixed-halide $n = 1$ RP phases with composition $\text{PEA}_2\text{PbI}_{4-x}\text{Br}_x$ ($x \leq 1.5$). A correlation between the PL emission peak and halide content is possible by taking literature data and extrapolating the bromine content over the reported emission energies (Figure S5).^{23,25} Using this correlation we estimate the bromide content to be $0.5 < x < 1.5$. The driving force for this alloying is likely the more negative formation energy of the alloyed phases compared to the pure-halide analogues (*i.e.*, PEA_2PbI_4 and $\text{PEA}_2\text{PbBr}_4$).²⁴ Lastly, the *iodine*- and *mixed*-PEABr samples seem to exhibit an inhomogeneous distribution of bromine within the RP phases. This is highlighted by the shift in the PL peak position when measurements are taken from a new sample spot, as depicted by the cyan dots in Figure 1g,h. This inhomogeneity explains the fluctuations in the PL peak maxima in *iodine*-PEABr and *mixed*-PEABr samples. Laser-induced halide migration may also contribute to these differences.

Structural characterization through XRD shows a predominance of $n = 1$ RP phases on top of all the samples, with peak position at $2\theta \cong 5.2^\circ$ for Cu K α radiation (Figure S6). Because of the similarity in the peak position for all $n = 1$ RP phases in our XRD data, we cannot tell apart iodine- or bromine-rich phases and, for that purpose, we used the PL peak positions. An important aspect revealed by XRD is the presence of unreacted salt on the surface of the PEAI-treated samples (Figure S7), as previously reported.^{7,11,34} This is consistent with the delayed formation of the RP phases observed in the PL color maps (Figure 1c,d). However, there is no evidence of PEABr salt in the XRD from Figure S6 (a diffraction peak should appear at $2\theta = 5.51^\circ$).³⁵ This suggests that PEABr reacts more readily with the 3D perovskites and is nearly completely consumed during the spin coating process, which is in agreement with the *in situ* PL color maps (Figure 1e,f). Again, this higher reactivity can be justified by the more negative formation energy of the alloyed RP phases. The difference in formation energy is -3 meV per halide atom for the formation of mixed-halide RP phases, in comparison to their phase-pure equivalents.²⁴ Accordingly, the intensity of the diffraction peaks of the RP phases from the PEABr-treated samples shows higher amounts of the $n = 1$ RP phase on top of the films than for PEAI-treated samples (note that the intensity in this case is comparable; see Materials and Methods for details and Figure S8). Finally, we demonstrate that the RP phase layers are oriented in parallel to the 3D perovskite film surface (Figures S8). This orientation is also supported by the

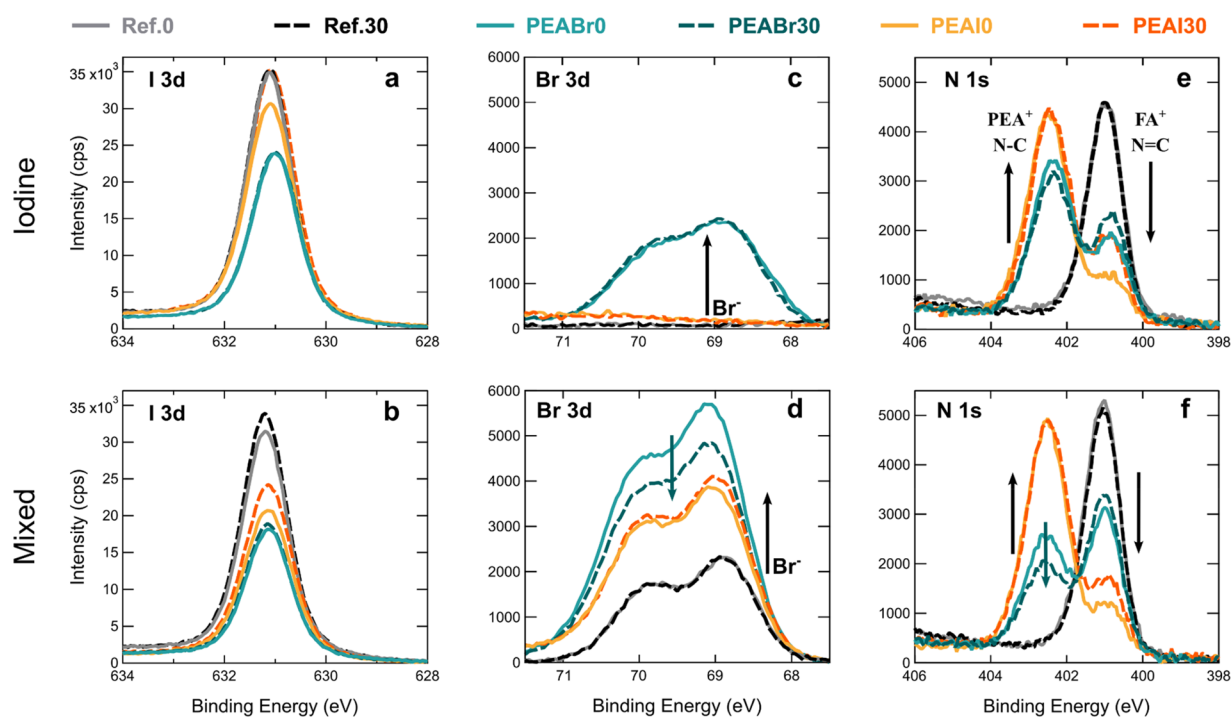


Figure 2. Surface-sensitive XPS spectra of specific elements before (solid lines) and after (dashed lines) annealing for 30 min. Annealed and nonannealed samples have the numbers 30 and 0 in their notations, respectively. *Iodine* samples are at the top row, and *mixed* samples at the bottom row. PEAI- and PEABr-treated samples are represented in orange and cyan colors, respectively. (a, b) I $3d_{3/2}$ peaks, (c, d) Br $3d$ peaks, and (e, f) N $1s$ peaks. Ref. denotes the pristine *iodine* or *mixed* perovskites, depending on the row. Black arrows show the main compositional variation of each species with respect to the references, and dark cyan arrows emphasize a particular observation in a given panel.

literature.^{16,36} The organic cation bilayer, separating the 3D and RP phases, likely mitigates most strain that could result from the 3D and 2D lattice mismatch.

The intense diffractions of $n = 1$ RP phase on top of PEABr-treated samples and the low intensity of its emission in the *in situ* PL maps reveal a difference between XRD and optical characterizations. A possible explanation for this may originate in the optical properties of the mixed-halide, $n = 1$ RP phases. It has been shown that the photoluminescence quantum-yield (PLQY) decreases significantly in tin-based, mixed-halide 2D perovskites.³⁷ This is likely true for lead-based analogues,²² as increased Stokes-shift and full width at half maximum (fwhm) of the emissions are observed in their mixed-halide phases^{23,24} (compare also panels in Figure 1c,d). The halide inhomogeneities in these materials seem to increase the nonradiative recombinations and coupling with phonons, leading to a decrease in PLQY.²³ These effects are more pronounced at higher temperatures, which explains the strong thermal quench of the emission observed in Figure 1c,d. In addition, there is nearly no signal of the emission from the mixed-halide RP phases in the HyPL spectra (Figure S4b). In contrast, XRD measurements are less sensitive to small amounts or small domains of other phases such as the $n = 2$ RP phases. Although *in situ* and HyPL show clear emission signals from the $n = 2$ RP phase for basically all samples, there is no evidence of this phase in the XRD (Figures S6 and S7; its (001) and (002) peaks should be close to $2\theta = 4^\circ$ and 8° , respectively).^{38,39} We attribute this divergence to the higher sensitivity of optical measurements to very small amounts of these luminescent materials⁷ and to different penetration depths of X-rays versus visible light. Therefore, optical measurements will be more sensitive to the surface, while X-rays will carry more

information from the bulk of the material. The detection sensitivity is even more pronounced in this case due to charge funneling among the RP phases, where even small domains of the lower-bandgap $n \geq 2$ RP phases may function as radiative recombination centers.^{21,40–42} Thus, optical or XRD measurements alone can be misleading to quantify and compare the RP phases on the surface of 2D/3D perovskites.

Surface-sensitive XPS measurements were conducted on the reference 3D perovskites, without RP phases, as well as on the 2D/3D stacks before and after annealing to assess the sample composition at the surface (Figures 2 and S9). Table S1 summarizes the relative elemental composition on the surface of the films compared to Pb, assuming that Pb is the least likely to migrate or diffuse in the system under study. After coating the 3D perovskites with PEAX salts, the intensity of Pb $4f$ peaks decrease, implying a lower Pb surface content compared to the reference samples due to the deposition of the salt and formation of the RP phases (Figure S9a,b). Except for the PEAI treated samples, the Pb $4f$ intensity is essentially constant before and after annealing. Similar decrease in intensity after the PEAX deposition is observed for the Cs $3d_{5/2}$ signal (Figure S9c,d).

The I $3d_{3/2}$ peak (Figure 2a) has an intensity similar to the peaks from the reference *iodine* perovskite, while the Pb signal decreases (Figure S9a). Thus, when PEAI is added, the I/Pb ratio increases by up to 25% (Table S1). Notably, the I/Pb ratio reveals a consistent iodine deficiency of about 20%, relative to the stoichiometry of both the 3D perovskite (APbI_3 , reference) and the $n = 1$ RP phase (PEA_2PbI_4 , *iodine*-PEAI). The treatment with PEAI also leads to a noticeable increase in the concentration of the carbon signal from PEA^+ cations, along with a shoulder at approximately 287 eV associated with

the C–N species (Figure S9e).^{31,43} This increase is observed for both PEAX salts. In the case of *iodine*-PEABr, there is a reduction in the intensity of the I 3d_{3/2} peak compared to other treatment conditions for the *iodine* perovskite. The I/Pb ratio for these samples indicates an approximate 40% iodine deficiency, assuming a PEA₂PbI₄ stoichiometry. This higher iodine deficiency compared to *iodine*-PEAI samples corroborates the formation of mixed-halide RP phases.

For the *mixed* perovskite, we observe a general reduction in I 3d_{3/2} peak intensity following treatment with both PEAX salts (Figure 2b). Notably, the I/Pb ratio for the *mixed*-PEAI samples shows a slight increase of about 10%, relative to the reference *mixed* perovskite. This aligns with the iodine migration into the crystalline structure of the *mixed* 3D perovskite, while bromine migrates to the surface and RP phases. In other words, this halide interdiffusion is the reason for the 10% rise in surface iodine concentration, compared to a 25% increase in its *iodine*-PEAI counterpart. The iodine diffusion into the *mixed* 3D perovskite is linked to the red shift observed in *in situ* PL (Figure S2d). Note that, in the case of the *iodine* samples, the perovskite core levels exhibit a small shift of roughly 0.1 eV toward lower binding energies after the deposition of the PEAX salts with respect to the core level position of the perovskite layer without PEAX treatment. While such a rigid peak shift of all core levels can be indicative of a change in Fermi level position in the gap (e.g., due to the passivation), the absolute value of the shifts is on the order of magnitude as the measurement error and can hence not be considered as statistically significant.

The Br 3d XPS peaks in the *iodine*-PEABr sample show an obvious increase in bromine content because of the PEABr treatment (Figure 2c). Also, a general increase in the bromine content is observed with the deposition of both PEAX salts on the *mixed* perovskite (Figure 2d and Table S1). This increase corresponds with the trends observed in I 3d_{3/2} XPS (Figure 2b), with bromine migration from the underlying *mixed* perovskite to the surface and iodine diffusing into the *mixed* perovskite. Similar halide interdiffusion has been reported for mixed-halide perovskites under visible light illumination.⁴⁴ Intriguingly, despite the higher bromine concentration, the Br/Pb ratio on the surface of the *mixed*-PEABr decreases by approximately 12% after annealing (see Table S1 and the dark-cyan arrow in Figure 2d).

Figure 2e,f shows two distinct XPS signals for the N 1s level: one, higher in energy, is associated with the N–C single bond from PEA⁺ cations, which is positively charged (+1), and a second one is related to the N–C double bond (N=C) in FA⁺ cations, where the positive charge is shared between the two nitrogen atoms (+1/2).^{14,31,43} Interestingly, the PEA⁺ content on the surface of the PEABr-treated samples is not as high as for PEAI treatment and also not constant upon annealing. In particular, a decrease in the PEA/Pb ratio by 25% is observed after the annealing of the *mixed*-PEABr sample (Table S1), which suggests a penetration of this species into the film (Figure 2f, dark-cyan arrow). It is well-known that anions and cations move in halide perovskites.^{45,46} For 2D/3D perovskite architectures explicitly, it was found that the bulky cation PEA⁺ moves into the 3D perovskite film.^{14,47} These bulky cations can possibly migrate along grain boundaries, assisted by mobile A-site point defects, for example.^{48,49} A transmission electron microscopy TEM study by Lee *et al.* supports the migration of PEA⁺ species across grain boundaries.⁴⁸

As we see a 12% decrease in the Br/Pb ratio in Figure 2d, we also speculate that Br is migrating into the 3D film. This migration possibly also occurs through the grain boundaries, as we do not observe an increase in the bandgap of the *mixed* 3D perovskites (Figure S2d). This hypothesis is supported by the work of deQuilettes *et al.*, where the authors show higher concentration of bromine at the grain boundaries upon hexylammonium bromide treatment, as revealed by scanning-TEM energy-dispersive X-ray elemental maps.⁵⁰ Migration at the grain boundaries have been reported to be the dominant mechanism in metal halide perovskites due to a much lower activation energy compared to the migration in grain interiors.^{51,52} The migration of Br through the grain boundaries may also be assisted by X-site point defects. Note that the Pb content is constant before and after annealing for *mixed* samples (Figure S9b), meaning that the changes in PEA/Pb and Br/Pb ratios are the reason for PEA⁺ and Br-surface concentration variations. Carbon 1s and Cs 3d_{5/2} XPS signals corroborate this interpretation.

In agreement with the N 1s peak, the C 1s XPS signal for PEABr-treated samples does not increase as much as for PEAI-treated ones after deposition of the salts (Figure S9e,f and Table S1). It also shows a decrease in the surface concentration after annealing (dark-cyan arrow in Figure S9f). In addition, the deposition of PEABr does not impact the XPS signal intensity of the A-site cations (FA⁺ and Cs⁺) to the same extent as the PEAI deposition does (Figure 2e,f and Figure S9c,d, respectively). In fact, the FA⁺ XPS signal intensity is even higher than the PEA⁺ signal in the *mixed*-PEABr sample (Figure 2f). These observations support the hypothesis of diffusibility of PEA⁺ into the 3D layer through the grain boundaries of the perovskite films. This phenomenon is only observed for PEABr-treated samples and is more evident on the *mixed* 3D perovskite.

Finally, the N 1s XPS also provides insights into the dynamics of the FA⁺ cations. Initially, the FA/Pb ratio decreases due to the deposition of the PEAX salts. However, after annealing, its intensity is partially restored in all cases (see last two columns in Table S1). This restoration of FA⁺ on the surface corroborates the formation of the *n* = 2 RP phase (i.e., PEA₂APb₂X₇, A = FA⁺ and Cs⁺) which is observed in the *in situ* PL and HyPL data (Figure 1c,d and Figure S4a,b, respectively). Furthermore, the distinct formation times of the *n* = 1 and *n* = 2 RP phases indicate that the *n* = 1 phase forms initially and, subsequently, the A-site cations migrate from the 3D perovskite to form the *n* = 2 RP phase. Cs⁺ may also be restored to the surface (Figure S9c,d) and can be partially incorporated in the *n* = 2 RP phases. With the Cs⁺ incorporation, the formation of the mixed-cation PEA₂FA_{1-x}Cs_xPb₂X₇ is more likely due to the low concentration of Cs⁺ relative to FA⁺ cations in the 3D perovskites. For the *mixed*-PEAI, we only detect this *n* = 2 phase in its HyPL spectrum with low intensity (Figure S4b). Similar diffusion of FA⁺ cations has been previously reported and has been associated with partial substitution of PEA⁺ with FA⁺ cations in PEA₂APb₂X₇ RP phases.¹⁴ This is also possible in our case, for both *n* = 1 and *n* = 2 RP phases, and it is likely happening concomitantly with the *n* = 2 RP phase formation.

Literature reports discuss A- and L-site cation diffusion in 2D/3D perovskites. Kamat and colleagues provide evidence of A-site cation migration from 3D to 2D perovskites.^{53,54} Even in physically paired films, the *n* = 1 RP phase film partially converts to *n* = 2 RP phase via A-site cation migration.⁵³ This

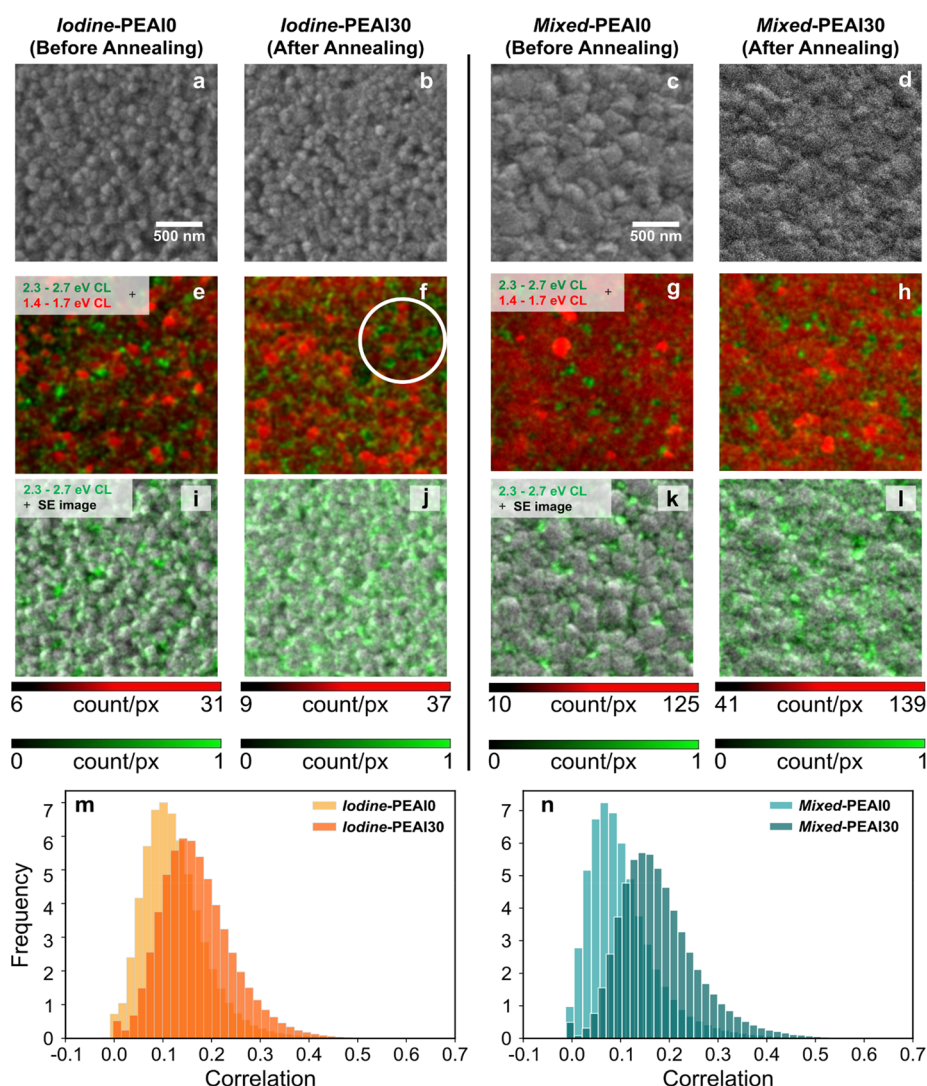


Figure 3. (a–d) Scanning electron microscopy, secondary-electron images of the *iodine*-PEAI and *mixed*-PEAI samples before and after 30 min annealing at 65 °C. Overlaid cathodoluminescence images of the 2D/3D films with different bandpass filters: 2.3–2.7 eV for the RP phases (green) and 1.4–1.7 eV for the 3D perovskites (red): (e) *iodine*-PEAI0; (f) *iodine*-PEAI30, white circle emphasizes a region with good coverage of RP phases; (g) *mixed*-PEAI0; and (h) *mixed*-PEAI30 samples. CL image overlaid with secondary electron (SE) image for (i) *iodine*-PEAI0, (j) *iodine*-PEAI30, (k) *mixed*-PEAI0, and (l) *mixed*-PEAI30 samples. Annealed and nonannealed samples have the numbers 30 and 0 in their notations, respectively. Image sizes: $2.5 \times 2.5 \mu\text{m}^2$ ($128 \times 128 \text{ px}^2$). Pixel dwell time: 20 μs . (m, n) LPIC histograms before and after annealing for *iodine*-PEAI and *mixed*-PEAI sample, respectively, with 2.3–2.7 eV bandpass filter.

migration is influenced by the L-site cation structure, with butylammonium (BA^+) showing a more favorable migration barrier than PEA^+ . L-site cation migration was unclear, but Seetharaman *et al.* reported evidence of such migration from RP phases in Sn-based 3D perovskites, also in physically paired films.⁵⁵ They also observed less favorable migration of PEA^+ cations compared to alkylammonium analogues, with PEA^+ migration occurring only under thermal and irradiation conditions due to increased steric hindrance. L-site migration in Pb-based 3D perovskites may be more difficult due to its lower thermal expansion and less active Pb $6s^2$ lone pair, responsible for local and long-range disorder in metal halide perovskites.^{56,57} In summary, our XPS data for PEABr-treated samples suggests PEA^+ diffusion into the underlying 3D perovskite film. Diffusion of these species has been demonstrated in several reports and for different cations such as octylammonium and butylammonium.^{14,47,53,54,58}

The lack of such diffusion in PEAI-treated samples, therefore, is an exception to what is generally observed. The reason behind this different behavior of PEAI- and PEABr-treated samples is possibly the lower reactivity of PEAI on the surface and its tendency to crystallize as unreacted salt (Figure S7). In addition, as shown in the XPS data, the iodine deficiency on the surface of the films may contribute to a prompt fixation of PEAI salt and related RP phase on the surface.

To analyze the radiative charge-carrier recombination behavior with submicrometer spatial resolution we carried out cathodoluminescence (CL) experiments on two selected samples, *iodine*-PEAI and *mixed*-PEAI, before and after annealing. The major difference between CL and PL is that charge carriers are excited via electrons instead of photons. Two bandpass filters were selected for the measurements: 2.3–2.7 eV (458–543 nm) for the RP phases and 1.4–1.7 eV (735–900 nm) for the 3D perovskites. It is noted that the

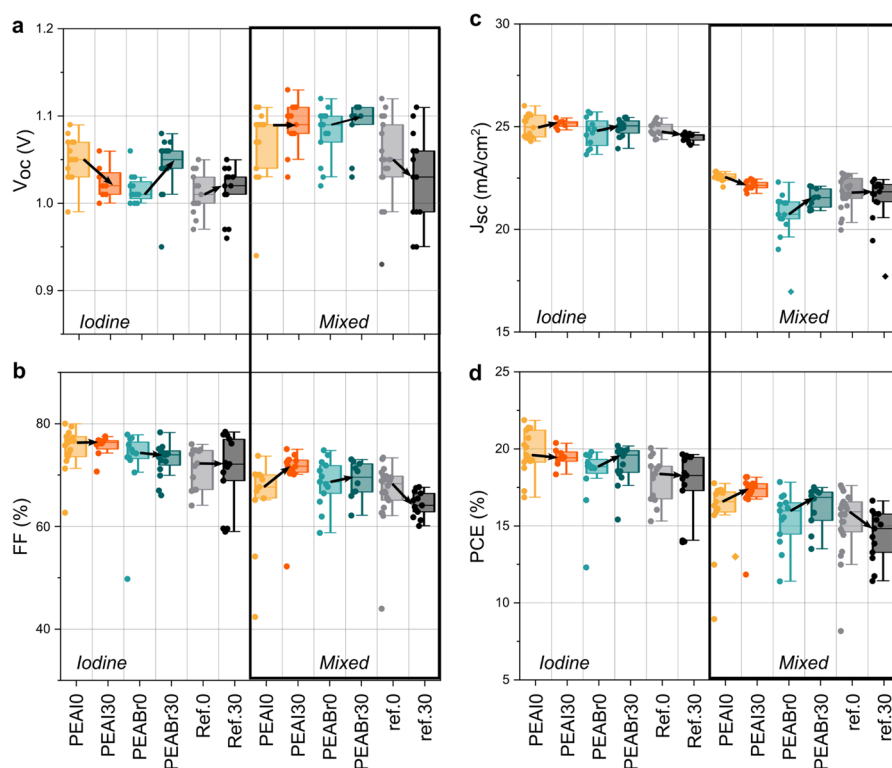


Figure 4. (a) Open-circuit voltage (V_{oc}), (b) fill factor, (c) short-circuit current density, and (d) power conversion efficiency (PCE) of the 2D/3D and reference PSCs before and after 30 min of annealing at 65 °C. Annealed and nonannealed samples have the numbers 30 and 0 in their notations, respectively. Solar cell parameters are extracted from the reverse J - V scans. The shaded area in the boxplots includes the 25th to the 75th percentile of the data. Median data value is presented as a solid line in the plot. The black arrows show the change in the median values from devices without to devices with annealing.

higher-energy bandpass filter also detects PbI_2 emission in addition to the RP phases' emission. The energy deposited by the electron beam at 3 kV extends roughly 90 nm into the 2D/3D stack.⁵⁹ More details are provided in [Materials and Methods](#). The secondary electron (SE) images ([Figure 3a–d](#) and [Figure S10](#)) show larger grain sizes for the *mixed* samples compared to the *iodine* samples. The morphology and grain size do not change significantly during annealing. Representative CL images from the 2D/3D perovskites are depicted in [Figure 3e–l](#), where red and green colors are assigned to the emissions from the 3D perovskite and RP phases, respectively. It is speculated that the bright green is related to PbI_2 emission, and the more diffuse green is related to RP emission.

Starting the discussion with the CL emission representative of the 3D perovskite films, it is apparent that the *iodine*-PEAI sample shows significant intensity variation (shades of red) before annealing and less variation after annealing ([Figure 3e,f](#) and [Figure S10](#)). These bright grains are possibly caused by differences in crystal quality where bright domains correspond to comparatively low nonradiative recombination rates.⁶⁰ Another explanation are inhomogeneities in the 3D perovskite composition due to some initial degree of phase segregation before annealing. For *mixed*-PEAI, halide segregation may be the reason for the red brighter spots, as the charge carriers are funneled to the iodine-richer phases with lower bandgap and recombine from these centers.^{29,30,61} After annealing, the emission of the 3D perovskites is more homogeneous in both cases, and the overall intensity of their emissions increases with annealing ([Figure 3f,h](#)). This observation corroborates the hypothesis of PEAX passivation, as the RP phases spread

through the grain boundaries and surfaces (white circle in [Figure 3f](#)).

Next, CL data from [Figure 3i–l](#) depicts emission from the 2.3–2.7 eV bandpass filter corresponding to the RP and/or PbI_2 phases overlaid with the SE images. It is worth mentioning that the emission of PbI_2 is highly intense in CL and, thus, it contributes to the CL signal when using the band filters for the RP phases (PbI_2 bandgap = 2.34 eV).⁶² Additionally, all 3D films were fabricated with PbI_2 -rich precursors. Initially, the emission is more concentrated at the grain boundaries, suggesting a more appreciable reaction of the PEAX salts with the excess PbI_2 on the surface of the films or at the grain boundaries' dangling bonds ([Figure 3i,k](#)). After annealing, the emission of the RP phases becomes more homogeneously distributed ([Figure 3j,l](#)), but intense green spots are still visible, which we speculate to be from excess PbI_2 . This effect is more pronounced for *mixed*-PEAI. Here, it is important to differentiate microscopic heterogeneity (seen in CL) from macroscopic homogeneity (seen with HyPL). The improved homogeneity after annealing is consistent with the mechanism extracted from *in situ* PL: initially, we form $n = 1$ phases with the reaction between PEAI and PbI_2 , and then the reaction continues with the 3D perovskites, with A-site incorporation into the RP phases.

To perform a more quantitative analysis, we measured the CL signal in different regions of the sample and used a local pixel intensity correlation (LPIC) function ([Figures S11 and S12](#)). The LPIC function subtracts the intensity of the pixel from the average of the eight neighboring pixels to indicate how the intensity of each pixel correlates to its neighbors (see [Materials and Methods](#)). Thus, the LPIC function provides a

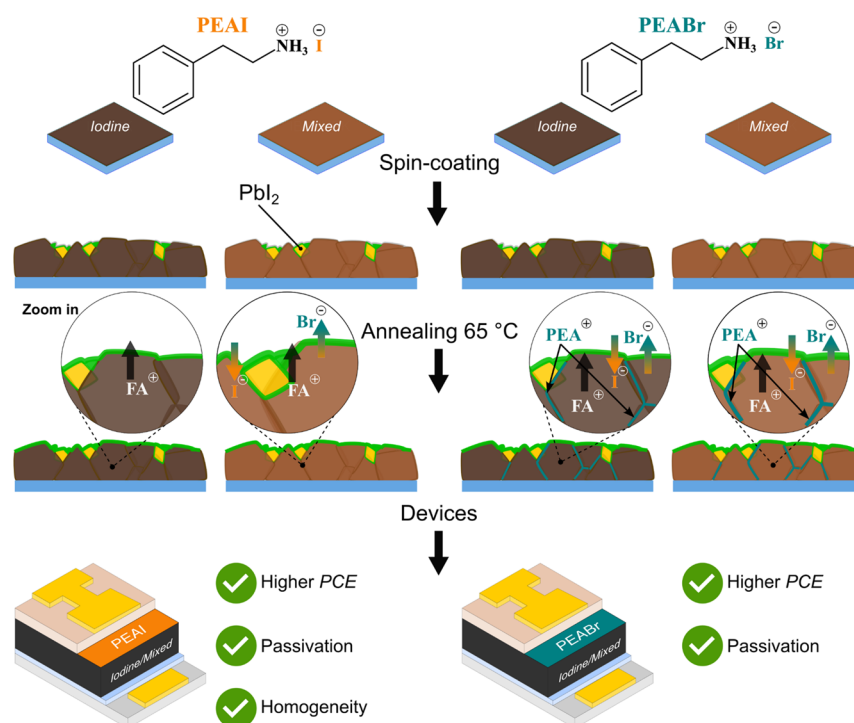


Figure 5. Schematics summarizing the migration pathways in 2D/3D perovskite stacks. Different halide compositions, pure-iodine and mixed-halide 3D perovskite films were combined with PEAI or PEABr (PEA = phenethylammonium) to form the 2D/3D perovskite interfaces.

quantitative metric for the degree of homogeneity of the overall emission in the form of a histogram as a function of the degree of nearest-neighbor correlation. Histograms of the LPIC function are depicted in Figure 3m,n. In both cases, the LPIC function confirms quantitatively what we observe qualitatively in the CL images of Figure 3i,l: upon annealing, the emission from the RP phases is more homogeneously distributed over the films.

We evaluated the impact of different 2D/3D interfaces on device performance by assembling solar cells as outlined in Materials and Methods. The architecture of the devices was FTO/TiO₂-c/TiO₂-mp3D-Perovskite/RP-phases/Spirol/Au, with reference devices lacking the RP phase layers. The device performance metrics are shown in Figure 4a–d (reverse) and Figure S13 (reverse and forward *J–V* scans).

Figure 4a reveals an improvement in open-circuit voltage (*V*_{OC}) compared to the reference when treating the 3D perovskites with PEAX salts, especially in the *mixed* perovskite cases. This can be associated with passivation of near-band-edge defects. The passivation of monoammonium halide salts is well-reported in the literature.^{11,13,15,63} The most significant *V*_{OC} improvements are observed for annealed *mixed*-PEAI and *mixed*-PEABr devices, in comparison to the annealed reference (60 and 70 mV, respectively). This could potentially be due to the interdiffusion of halides, which, in conjunction with the formation of the 2D/3D interface, results in effective defect passivation or improvement of the band alignment. Higher diffusibility through grain boundaries or reactivity of PEA⁺/PEABr species may contribute to a more effective passivation of the annealed *mixed*-PEABr (the highest *V*_{OC}, 1.10 V).

Despite the effective passivation offered by both PEAX salts, Figure 4d shows higher PCE for PEAI-treated devices, both pre- and postannealing, with best PCE of 21.86% for *iodine*-PEAI0 and 18.18% for *mixed*-PEAI30. This hints to a

combined contribution of the unreacted PEAI salt and related RP phases to device efficiency, in agreement with previous reports on PEAI and PEA₂PbI₄ passivation.^{11,48,64} Annealed *iodine*- and *mixed*-PEAI samples also showed a narrower fill factor (FF) distribution and highest short-circuit current density (*J*_{SC}), indicating an improved charge extraction (Figure 4b,c). A decrease in the *V*_{OC} of *iodine*-PEAI30 devices is observed, despite the increase of the *V*_{OC} in *iodine*-PEA0. This happens because there is a difference between passivation *via* unreacted PEAI salt and the RP phase. Before annealing, the passivation is mainly due to the unreacted PEAI salt.¹¹ Upon annealing, the passivation is due to the PEA₂PbI₄ RP phase. However, we also form some *n* = 2 RP phase in the case of the *iodine*-PEAI30 sample. The passivation of *n* = 2 phase is not as effective as for PEA₂PbI₄, although it improves the FF and *J*_{SC} due to a more effective charge separation and extraction.⁷ Lastly, the *n* = 2 RP phase is also less insulating compared to the *n* = 1.^{65,66} Although there is a complex interplay and multiple overlapping effects upon 2D passivation, in general we observe improvement in the device performance and statistical distribution of the photovoltaic parameters in all annealed PEAI-treated devices.

Devices treated with PEABr also showed higher PCE compared to the references, particularly in annealed samples. Interestingly, prolonged annealing worsened parameters in pristine *mixed* 3D perovskites devices, likely due to increased halide segregation and structural defects. PEABr treatment appears to mitigate this degradation, enhancing device performance.

In this study, annealed *iodine*- and *mixed*-PEAI devices presented the best trade-off between efficiency and reproducibility. Different halides and ammonium salts yielded varying results. For instance, Sutanto *et al.*¹⁷ reported superior solar cells using bromide anion for TMA⁺ cations, while Liu *et al.*¹⁶

found that treatment with neoPA^+ and Cl^- outperformed devices treated with neoPAI and neoPABr . Regardless, all 2D perovskites formed were predominantly, if not entirely, iodine-based. Thus, the effect of the halide is influenced by the structure of the L-site cation and the composition of the underlying 3D perovskites. Due to this variability, it is challenging to establish general trends in 2D/3D perovskites fabricated with solution deposition of ammonium halide salts.

Figure 5 summarizes our findings regarding the migration at the 2D/3D interfaces investigated here. (1) Spin coating of the PEAX dissolved in IPA onto the 3D perovskite films leads to incomplete and heterogeneous coverage of the RP phases on the microscopic scale, although HyPL shows even coverage of the RP phases throughout the film (macroscopic scale). In the case of PEAI, some of the salt remains unreacted even after annealing (Figure S7). XRD suggests that the reaction with PEABr is more favorable toward the formation of the RP phases in both *iodine* and *mixed* perovskites. This might be related to a lower formation energy of the mixed-halide 2D perovskite compared to their phase-pure counterparts (PEA_2PbI_4 and $\text{PEA}_2\text{PbBr}_4$). (2) Upon heat treatment the reaction between the PEAX salts, excess $\text{PbI}_2/\text{PbBr}_2$, and the 3D perovskites continues. In all cases, the reaction results in $n = 1$ and $n = 2$ RP phases, leading to a more homogeneous coverage of the 3D layers in the micrometric scale. (3) Three migration trends are evident. XPS data reveals that upon annealing, FA^+ and Cs^+ cations partially return to the film surface, triggering the formation of $n = 2$ RP phases. It also shows PEA^+ cations penetrating 3D perovskites when films are coated with PEABr, a phenomenon not seen with PEAI. Both PEA^+ and bromine appear to diffuse into the film, possibly explaining the low bromine intake by the RP phases and the absence of PEABr salt diffractions in the XRD. An interplay between surface iodine deficiency and lower reactivity of PEAI compared to PEABr may be the reason for the lack of PEA^+ diffusion in PEAI-treated samples.

Based on our findings and literature reports on the dynamic nature of the 2D/3D interface, two effects seem to affect the performance and stability of devices treated with L-site cations: diffusion of the L-site cations and reconstruction of the perovskite surface, with formation of higher- n phases; and halide mixing at the interface, with diffusion from the 2D layer into the 3D and vice versa. As such, we propose here a few strategies that could help enhance the stability of perovskite devices incorporating surface treatments with L-site cations: (i) engineering cations to reduce their reactivity with the underlying perovskite;⁶⁷ (ii) use cations with mixed halide counterions to avoid halide exchange between the 3D bulk and the 2D surface layer; (iii) develop nonhalide counterions to pair with the cations used for surface passivation; and (iv) develop further the use of Dion-Jacobson (DJ) 2D/3D perovskites, as the doubly charged L-site cations in this case can slow down their migration under thermal stress.⁶⁸

To conclude, we explored how the properties of 2D/3D perovskite interfaces change based on the halide selection in PEAX salts and the halide composition of the underlying 3D perovskite. We found that these interfaces exhibit complex ionic dynamics under thermal stress. Initially, after coating the PEAX salts, the RP phases are distributed unevenly on the surface at a microscopic level, with some residual unreacted salt persisting on the PEAI-treated samples. However, annealing leads to a more uniform coverage, which indicates high ionic mobility at the 2D/3D interface. Three main

migration behaviors were observed: (i) bromine from *mixed* perovskites diffuses to the film's surface while iodine migrates inwardly when treated with PEAX salts; (ii) PEA^+ (associated with PEABr) penetrates through the grain boundaries upon annealing, which is not seen with PEAI; and (iii) thermal treatment partially restores A-site cations from the 3D perovskites to the surface, leading to the formation of minority $n = 2$ RP phases. Despite the improved performance and stability of 2D/3D perovskite solar cells, in this work and literature reports, our findings highlight the dynamic nature of these interfaces and validate the importance of thermal annealing to achieve more homogeneous interfaces. Notably, the mobility of PEA^+ suggests that even bulky cations can diffuse within the 2D/3D interface, potentially affecting the long-term stability of devices. Therefore, while 2D/3D perovskites hold promise for stable photovoltaics, optimizing these interfaces remains a challenge. The complex migration behavior and compositional dependence described here suggest that generalized statements about 2D/3D interfaces seem difficult at this point and more studies are needed.

MATERIALS AND METHODS

Phenethylammonium bromide ($\geq 98\%$), phenethylammonium iodide, anhydrous $\text{N,N}'$ -dimethylformamide (99.8%), anhydrous dimethyl sulfoxide ($\geq 99.9\%$), anhydrous chlorobenzene (99.8%), anhydrous isopropanol (99.5%), acetylacetone (99%), titanium di-isopropoxide bis(acetylacetonate) (75% in 2-propanol), anhydrous ethanol (99.9%), TiO_2 paste, bis-(trifluoromethane)sulfonimide lithium salt, FK209Co (98%), and acetonitrile (anhydrous) were purchased from MilliporeSigma and used as received. Lead iodide (99.99%, trace metals basis; for perovskite precursor) and lead bromide ($>98.0\%$, for perovskite precursor) were purchased from TCI America and used as received. Spiro-OMeTAD was purchased from 1-Material.

Perovskite Thin-Film Fabrication. Thin films were deposited on 1×1 in, on soda lime glass substrates.

$\text{Cs}_{1/6}\text{FA}_{5/6}\text{PbI}_3$. The masses of PbI_2 , FAI, and CsI precursors were weighed in different vials to prepare a 1.2 M $\text{Cs}_{1/6}\text{FA}_{5/6}\text{PbI}_3$ solution with 5% excess PbI_2 . The PbI_2 solution was prepared first, in DMF:DMSO (2:1) ratio, and stirred at 85°C for 1 h. Once the PbI_2 was fully dissolved, the PbI_2 solution is transferred to the FAI vial. After the full solvation of FAI, the solution was transferred to the CsI vial, and the mixture was stirred until complete dissolution of the salt at room temperature. For the film preparation, $45 \mu\text{L}$ of the as-prepared solution was used with a two-step static spin process: 1000 rpm, 1000 rpm/s, for 10 s; followed by 6000 rpm, 6000 rpm/s, for 20 s. An aliquot of $250 \mu\text{L}$ of chlorobenzene was dripped onto the spinning film at 28 s from the start of the spin-coating, taking about 1 s to drip the antisolvent. The as-cast perovskite film was subsequently annealed at 150°C for 10 min.

$\text{Cs}_{1/6}\text{FA}_{5/6}\text{PbI}_{2.5}\text{Br}_{0.5}$. A similar procedure was carried out to prepare a 1.2 M $\text{Cs}_{1/6}\text{FA}_{5/6}\text{PbI}_{2.5}\text{Br}_{0.5}$ perovskite solution. The PbI_2 , PbBr_2 , FAI, and CsI precursors were weighed in different vials. The precursors were dissolved in the following order: $\text{PbI}_2 \rightarrow \text{FAI} \rightarrow \text{PbBr}_2 \rightarrow \text{CsI}$, using DMF:DMSO (2:1) and a 5% excess of PbI_2 and PbBr_2 (mol %). Each solution is transferred to the next vial until complete dissolution of the salts. The same spin and annealing recipe was used as for $\text{Cs}_{1/6}\text{FA}_{5/6}\text{PbI}_3$.

Surface-Treated Films. PEAI and PEABr 20 mM in IPA solutions were prepared (5 and 4.05 mg/mL, respectively). 80 μL were dynamically spun on the perovskite surface at 5000 rpm, 5000 rpm/s, for 20 s (~ 2 s after the beginning of the rotation), either without annealing or with annealing for 30 min at 65 $^{\circ}\text{C}$ right after the deposition.

In Situ PL. The in situ PL measurements were carried out using a home-built setup in an N_2 -filled glovebox. Excitation was performed using a laser diode emitting at 405 nm, and the PL emission was collected using an optical fiber coupled with an Ocean Optics spectrometer (“Flame”) calibrated by the manufacturer. A Jacobian correction was applied to the data transforming them from wavelength- to energy-space, and a linear background was removed before fitting the spectra using a combination of 1–3 Gaussians, depending on the presence of RP phases. The integration time for each spectrum was 500 ms during annealing, with a laser power of approximately 5 mW/ cm^2 . Immediately after finishing the surface treatment of the films with PEAX salts, the films were annealed for 30 min at 65 $^{\circ}\text{C}$. Before placing them on the hot plate, the measurements were initialized, and the films were placed into the focal point of the laser on the hot plate.

Hyperspectral PL. The hyperspectral PL setup consists of a hyperspectral imager Grand-EOS from PhotonEtc equipped with a CMOS camera (Orca-Flash 4.0 v3 from Hamamatsu) which allows for acquiring large-size images (15 \times 15 cm^2) with a resolution of 133 μm per pixel. Spectral acquisitions were done in the range of 500–1000 nm with a spectral resolution of 2 nm. The samples are uniformly illuminated with LEDs at a wavelength of 405 nm under a fluence of 70 mW/ cm^2 . The integration time for the measurements was 1 s. Experimental data were acquired using PHySpecV2 software resulting in a three-dimensional (x, y, l) datacube with both spatial and spectral features. For the images shown in Figure S3, intensity maps at the respective wavelength (resolution 2 nm) were extracted.

X-ray Diffraction (XRD). XRD measurements were performed in a Bruker AXS D8-Discover X-ray Diffractometer. The source used was Co $K\alpha$ radiation ($\lambda = 1.7902 \text{ \AA}$). All the diffractograms were reported converting the wavelength to the more commonly used Cu $K\alpha$ radiation ($\lambda = 1.5406 \text{ \AA}$). The measurements were carried out with a Bragg–Brentano geometry with an area detector. The initial incidence and detection angles were 5 $^{\circ}$ and 15 $^{\circ}$, respectively. The whole measurement was performed with three frames where source and detector increased by 5 $^{\circ}$ /frame each, with ending positions at 15 $^{\circ}$ and 25 $^{\circ}$, respectively. Because the 2D materials are oriented on the surface of the samples (planes parallel to the film), the integrated XRD profile corresponds to 100% of their diffraction intensity, and so we can roughly say that the amount of RP phases on top of the film is proportional to the diffraction intensity. For this experiment, we set the sample stage to oscillate in a way that the films moved 4 mm in x and 4 mm in y directions while measuring. This way we could have an averaged signal of a larger area of the films. The integration time for each frame was 300 s (total of 900 s for the whole measurement).

X-ray Photoelectron Spectroscopy (XPS). XPS spectra are measured within a Kratos Axis Ultra system using a monochromatic Al $K\alpha$ source and a hemispherical electron energy analyzer (3×10^{-8} Torr). Spectra of various core levels with 0.05 eV resolution and survey scans with 1 eV resolution were acquired. Depending on the signal-to-noise ratio, 4–8

sweeps are averaged. Samples were grounded for measurements and did not show charging effects. Slight mismatches in binding energies were corrected using the Pb peak position.

Scanning Electron Microscopy (SEM) and Cathodoluminescence (CL) Imaging. Secondary electron images and cathodoluminescence (CL) images are acquired with a home-modified Zeiss Gemini SUPRA 55 S2 Scanning Electron Microscope at the Molecular Foundry. An aluminum parabolic reflector is positioned above the sample in order to couple a 1.3 π sr solid angle of emission into photomultiplier tubes (Hamamatsu, H7360 and H7421-40) using a 458 and 543 nm dichroics and subsequent 735 nm long pass filter to separate the color channels into ranges 458 to 543 and 735 nm to beyond. All CL images were acquired on a freshly exposed area, by first blanking the electron beam and moving to the region of interest before recording an image. All CL images were acquired at 3 kV and at a beam current of ~ 10 pA with 512 \times 512 pixels and a scanning rate of 20 μs /pixel. The total image acquisition per region of interest took 5.24 s.

Analysis of CL Images. SE images obtained in tandem with CL images collected were analyzed using open-source ImageJ. First, the raw CL images and SE images were Gaussian blurred (2 pixels for 458–543 nm CL channel and 1 pixel for both SE and 735–900 nm CL channel images). The intensity of each image is auto-adjusted using imageJ, followed by creating a multichannel composite to combine the adjusted images to provide a comprehensive visualization of the intensity distributions. For detailed CL image analysis, Gaussian filtered 32 bit CL images are used. The pixel intensity histograms and local pixel intensity correlation map were obtained using custom Python scripts. The local pixel intensity correlation map shows the correlation between central pixels and their eight adjacent pixels in a 3 \times 3 neighborhood, by subtracting eight times the central pixel intensity from the sum of 8 neighboring pixels. This shows how each pixel’s value correlates with its neighbors, capturing short-range intensity inhomogeneity. The correlation of the pixels on the image boundaries are set to 0.

Photovoltaic Device Fabrication. Substrates of glass measuring 1 in \times 1 in with a patterned thin film of FTO (sheet resistance of 7 $\Omega \text{ sq}^{-1}$) were meticulously cleaned through a series of steps. The cleaning process included a 15 min sonication in a 2% Hellmanex solution in deionized-water, followed by sequential rinses with deionized water, acetone, and isopropanol for 10 min each in the sonicator. The cleaned substrates were rapidly dried with a nitrogen gun and placed onto a hot plate in preparation for the subsequent deposition of the electron-transport layer. To isolate the active area of the pixels, glass slides were placed along the edges of each substrate, leaving them exposed. The hot plate temperature was set to 450 $^{\circ}\text{C}$. A layer of compact TiO_2 (referred to as $\text{TiO}_2\text{-c}$) was then applied using spray pyrolysis. This involved a solution made up of 480 μL of acetylacetone (Sigma-Aldrich), 720 μL of titanium di-isopropoxide bis(acetylacetonate) (75% in 2-propanol, Sigma-Aldrich), and 10.8 mL of 99.9% pure anhydrous ethanol (Sigma-Aldrich). Oxygen flowed at a rate of 3.5 L min^{-1} as the carrier gas for the spray. A Sparmax spray gun was utilized for the process, with approximately 10 s intervals between cycles and a 30 s delay in between. The spraying continued until the solution was exhausted. Substrates were then maintained at 450 $^{\circ}\text{C}$ for 30 min and allowed to cool to room temperature.

For the mesoporous TiO₂ film (referred to as TiO₂-mp), a solution of TiO₂ paste (consisting of 30 nm nanoparticles, GreatSolar) in 99.9% pure anhydrous ethanol (Sigma-Aldrich) was spin-coated onto the substrates. Spin-coating was performed at 2000 rpm, with an acceleration of 2000 rpm s⁻¹, for a duration of 10 s. Magic tape was applied to prevent deposition on the contacts during the spin-coating process. The coated substrates were swiftly transferred to a 100 °C hot plate for drying, lasting more than 10 min. The mesoporous film was subsequently sintered by gradually raising the temperature to 450 °C and maintaining it for 30 min. After a partial cooldown, while the substrates were still around 150 °C, they were moved to a glovebox with oxygen and water concentrations below 10 ppm. The deposition of the perovskite and passivation layer was performed on TiO₂-covered substrates, as described in [Perovskite Thin-Film Fabrication](#).

A spiro-OMeTAD solution in CB was prepared right before it was deposited to minimize aggregation in solution. This solution contained 28.4 mg of spiro-OMeTAD, 14.5 μL of Co (II) salt (FK209, Sigma-Aldrich, 300 mg mL⁻¹ stock solution in acetonitrile), 8.8 μL of Li-TFSI (Sigma-Aldrich, 520 mg mL⁻¹ stock solution in acetonitrile), and 14.4 μL of *tert*-butylpyridine (Sigma-Aldrich). The spin-coating parameters were set at 3000 rpm, with an acceleration of 3000 rpm s⁻¹, for a duration of 30 s. Around 80 μL of the spiro-OMeTAD solution was dripped onto the substrate at approximately 1 s after the spin-coating began. Prior to Au deposition, any CsFAMA and spiro-OMeTAD films present on the substrate edges were removed using cotton swabs moistened with DMF and acetonitrile, respectively. Finally, a layer of gold, approximately 60 nm thick, was thermally evaporated to serve as the top contact for the device.

Photovoltaic Device Characterization. The photovoltaic performance assessment was conducted utilizing a Fluxim Litos Lite arrangement, which featured a Wavelabs Sinus-70 AAA solar simulator that produced an AM1.5 spectrum for excitation purposes. The current–voltage (*J*–*V*) attributes were obtained through both forward and reverse scans, each performed at a scan rate of 50 mV s⁻¹. Stabilized power output measurements were completed utilizing a maximum power point (MPP) tracking algorithm over a span of 60 s. Prior to the measurement, the devices were not subjected to any preconditioning. To define a pixel area of 0.0625 cm², masking was employed during the measurements. Nitrogen gas was introduced into the measurement chamber throughout the characterization process, and no temperature regulation was implemented.

■ ASSOCIATED CONTENT

SI Supporting Information

The Supporting Information is available free of charge at <https://pubs.acs.org/doi/10.1021/acsenenergylett.4c00728>.

Schematic of *in situ* PL measurements; HyPL images and integrated PL curves; XRD measurements, fits, and detector images; additional XPS data; SEM and additional CL images and data; forward and reverse photovoltaic parameters ([PDF](#))

■ AUTHOR INFORMATION

Corresponding Authors

Carlo A. R. Perini – School of Materials Science and Engineering, Georgia Institute of Technology, Atlanta, Georgia 30332, United States; Email: cperini8@gatech.edu

Juan-Pablo Correa-Baena – School of Materials Science and Engineering, Georgia Institute of Technology, Atlanta, Georgia 30332, United States; orcid.org/0000-0002-3860-1149; Email: jpcorrea@gatech.edu

Carolyn M. Sutter-Fella – Molecular Foundry Division, Lawrence Berkeley National Laboratory, Berkeley, California 94720, United States; orcid.org/0000-0002-7769-0869; Email: csutterfella@lbl.gov

Authors

Raphael F. Moral – Nevada Extreme Conditions Laboratory, University of Nevada, Las Vegas, Las Vegas, Nevada 89154, United States; Molecular Foundry Division, Lawrence Berkeley National Laboratory, Berkeley, California 94720, United States; orcid.org/0000-0002-1844-4035

Tim Kodalle – Molecular Foundry Division, Lawrence Berkeley National Laboratory, Berkeley, California 94720, United States; Advanced Light Source, Lawrence Berkeley National Laboratory, Berkeley, California 94720, United States

Ahyoung Kim – Department of Chemistry, University of California, Berkeley, California 94720, United States

Finn Babbe – Chemical Science Division, Lawrence Berkeley National Laboratory, Berkeley, California 94720, United States; orcid.org/0000-0002-9131-638X

Nao Harada – Institut Photovoltaïque d'Île-de-France (IPVF), Palaiseau 91120, France

Javid Hajhemati – Institut Photovoltaïque d'Île-de-France (IPVF), Palaiseau 91120, France; CNRS, UMR 9006, Institut Photovoltaïque d'Île-de-France (IPVF), Ecole Polytechnique - IP Paris, Chimie Paristech - PSL, Palaiseau 91120, France

Philip Schulz – Institut Photovoltaïque d'Île-de-France (IPVF), Palaiseau 91120, France; CNRS, UMR 9006, Institut Photovoltaïque d'Île-de-France (IPVF), Ecole Polytechnique - IP Paris, Chimie Paristech - PSL, Palaiseau 91120, France; orcid.org/0000-0002-8177-0108

Naomi S. Ginsberg – Chemical Science Division, Molecular Biophysics and Integrated Bioimaging Division, and Materials Science Division, Lawrence Berkeley National Laboratory, Berkeley, California 94720, United States; Department of Chemistry, University of California, Berkeley, California 94720, United States; Department of Physics, University of California, Berkeley, California 94720, United States; STROBE, NSF Science & Technology Center, Berkeley, California 94720, United States; Kavli Energy NanoSciences Institute, Berkeley, California 94720, United States; orcid.org/0000-0002-5660-3586

Shaul Aloni – Molecular Foundry Division, Lawrence Berkeley National Laboratory, Berkeley, California 94720, United States

Craig P. Schwartz – Nevada Extreme Conditions Laboratory, University of Nevada, Las Vegas, Las Vegas, Nevada 89154, United States

Complete contact information is available at:

<https://pubs.acs.org/doi/10.1021/acsenenergylett.4c00728>

Author Contributions

Conceptualization, C.A.R.P., J.-P.C.-B., C.M.S.-F.; **software/analysis codes**, T.K., S.A.; **experimentation**, R.F.M., C.A.R.P., T.K., A.K., F.B., N.H.; **formal analysis**, C.A.R.P., T.K., R.F.M., A.K., N.H., J.H.; **data curation**, C.A.R.P., T.K., N.H., J.H., A.K., R.F.M., C.M.S.-F.; **writing original draft**, R.F.M., C.M.S.-F.; **writing - review and editing**, all authors have read and contributed to the draft; **visualization**, R.F.M., C.A.R.P., T.K., C.M.S.-F.; **supervision**, C.M.S.-F., C.P.S., N.S.G., P.S., J.-P.C.-B.; **funding acquisition**, J.-P.C.-B., C.P.S., C.M.S.-F.

Notes

The authors declare no competing financial interest.

ACKNOWLEDGMENTS

Work at the Molecular Foundry was supported by the Office of Science, Office of Basic Energy Sciences, of the U.S. Department of Energy under Contract No. DE-AC02-05CH11231. C.P.S. and R.F.M. acknowledge the support of the Chemical Sciences, Geosciences and Biosciences Division as well as EPSCoR through the grant DE-SC0023397. C.A.R.P. and J.-P.C.-B. acknowledge the support of the National Aeronautics and Space Administration (Award #80NSSC19M0201). This work was performed in part at the Georgia Tech Institute for Electronics and Nanotechnology, a member of the National Nanotechnology Coordinated Infrastructure (NNCI), which is supported by the National Science Foundation (ECCS-2025462). CL characterization was supported by STROBE, A National Science Foundation Science & Technology Center under Grant No. DMR 1548924. CL analysis was supported by the Center for Computational Study of Excited State Phenomena in Energy Materials (C2SEPEM) under the U.S. Department of Energy, Office of Science, Basic Energy Sciences, Materials Sciences and Engineering Division under contract no. DE-AC02-05CH11231, as part of the Computational Materials Sciences Program. N.S.G. also acknowledges a David and Lucile Packard Foundation Fellowship for Science and Engineering. This work was also supported by the French government in the framework of the program of investments for the future (Programme d'Investissement d'Avenir ANR-IEED-002-01). T.K. acknowledges funding by the US Department of Energy (DOE), Office of Science, Office of Basic Energy Sciences, Materials Sciences and Engineering Division, under contract no. DE-AC02-05-CH11231 (D2S2 program KCD2S2). P.S., N.H., J.H., C.M.S.-F., and T.K. thank the France-Berkeley Fund for funding support to enable travel to France.

REFERENCES

- (1) Metcalf, I.; Sidhik, S.; Zhang, H.; Agrawal, A.; Persaud, J.; Hou, J.; Even, J.; Mohite, A. D. Synergy of 3D and 2D Perovskites for Durable, Efficient Solar Cells and Beyond. *Chem. Rev.* **2023**, *123* (15), 9565–9652.
- (2) Yoo, J. J.; Seo, G.; Chua, M. R.; Park, T. G.; Lu, Y.; Rotermund, F.; Kim, Y.-K.; Moon, C. S.; Jeon, N. J.; Correa-Baena, J.-P.; Bulović, V.; Shin, S. S.; Bawendi, M. G.; Seo, J. Efficient Perovskite Solar Cells via Improved Carrier Management. *Nature* **2021**, *590* (7847), 587–593.
- (3) Chen, Y.; Zhang, M.; Li, F.; Yang, Z. Recent Progress in Perovskite Solar Cells: Status and Future. *Coatings* **2023**, *13* (3), 644.
- (4) Jena, A. K.; Kulkarni, A.; Miyasaka, T. Halide Perovskite Photovoltaics: Background, Status, and Future Prospects. *Chem. Rev.* **2019**, *119* (5), 3036–3103.
- (5) Azmi, R.; Ugur, E.; Seitkhan, A.; Aljamaan, F.; Subbiah, A. S.; Liu, J.; Harrison, G. T.; Nugraha, M. I.; Eswaran, M. K.; Babics, M.;

Chen, Y.; Xu, F.; Allen, T. G.; Rehman, A. U.; Wang, C.-L.; Anthopoulos, T. D.; Schwingenschlögl, U.; De Bastiani, M.; Aydin, E.; De Wolf, S. Damp Heat–Stable Perovskite Solar Cells with Tailored-Dimensionality 2D/3D Heterojunctions. *Science* **2022**, *376* (6588), 73–77.

(6) Sutanto, A. A.; Szostak, R.; Drigo, N.; Quelo, V. I. E.; Marchezi, P. E.; Germino, J. C.; Tolentino, H. C. N.; Nazeeruddin, M. K.; Nogueira, A. F.; Grancini, G. In Situ Analysis Reveals the Role of 2D Perovskite in Preventing Thermal-Induced Degradation in 2D/3D Perovskite Interfaces. *Nano Lett.* **2020**, *20* (5), 3992–3998.

(7) Kodalle, T.; Moral, R. F.; Scalón, L.; Szostak, R.; Abdelsamir, M.; Marchezi, P. E.; Nogueira, A. F.; Sutter-Fella, C. M. Revealing the Transient Formation Dynamics and Optoelectronic Properties of 2D Ruddlesden-Popper Phases on 3D Perovskites. *Adv. Energy Mater.* **2023**, *13* (33), No. 2201490.

(8) de Holanda, M. S.; Moral, R. F.; Marchezi, P. E.; Marques, F. C.; Nogueira, A. F. Layered Metal Halide Perovskite Solar Cells: A Review from Structure-Properties Perspective towards Maximization of Their Performance and Stability. *EcoMat* **2021**, *3* (4), No. e12124.

(9) Yu, Y.; Liu, R.; Liu, C.; Shi, X.-L.; Yu, H.; Chen, Z.-G. Synergetic Regulation of Oriented Crystallization and Interfacial Passivation Enables 19.1% Efficient Wide-Bandgap Perovskite Solar Cells. *Adv. Energy Mater.* **2022**, *12* (33), No. 2201509.

(10) Yoo, J. J.; Wieghold, S.; Sponseller, M. C.; Chua, M. R.; Bertram, S. N.; Hartono, N. T. P.; Tresback, J. S.; Hansen, E. C.; Correa-Baena, J.-P.; Bulović, V.; Buonassisi, T.; Shin, S. S.; Bawendi, M. G. An Interface Stabilized Perovskite Solar Cell with High Stabilized Efficiency and Low Voltage Loss. *Energy Environ. Sci.* **2019**, *12* (7), 2192–2199.

(11) Jiang, Q.; Zhao, Y.; Zhang, X.; Yang, X.; Chen, Y.; Chu, Z.; Ye, Q.; Li, X.; Yin, Z.; You, J. Surface Passivation of Perovskite Film for Efficient Solar Cells. *Nat. Photonics* **2019**, *13* (7), 460–466.

(12) Jang, Y.-W.; Lee, S.; Yeom, K. M.; Jeong, K.; Choi, K.; Choi, M.; Noh, J. H. Intact 2D/3D Halide Junction Perovskite Solar Cells via Solid-Phase in-Plane Growth. *Nat. Energy* **2021**, *6* (1), 63–71.

(13) Cho, K. T.; Zhang, Y.; Orlandi, S.; Cavazzini, M.; Zimmermann, I.; Lesch, A.; Tabet, N.; Pozzi, G.; Grancini, G.; Nazeeruddin, M. K. Water-Repellent Low-Dimensional Fluorous Perovskite as Interfacial Coating for 20% Efficient Solar Cells. *Nano Lett.* **2018**, *18* (9), 5467–5474.

(14) Perini, C. A. R.; Rojas-Gatjens, E.; Ravello, M.; Castro-Mendez, A.; Hidalgo, J.; An, Y.; Kim, S.; Lai, B.; Li, R.; Silva-Acuña, C.; Correa-Baena, J. Interface Reconstruction from Ruddlesden–Popper Structures Impacts Stability in Lead Halide Perovskite Solar Cells. *Adv. Mater.* **2022**, *34* (51), No. 2204726.

(15) ASutanto, A. A.; Drigo, N.; EQuelo, V. I. E.; Garcia-Benito, I.; Kirmani, A. R.; Richter, L. J.; Schouwink, P. A.; Taek Cho, K.; Paek, S.; Khaja Nazeeruddin, M.; Grancini, G. Dynamical Evolution of the 2D/3D Interface: A Hidden Driver behind Perovskite Solar Cell Instability. *J. Mater. Chem. A* **2020**, *8* (5), 2343–2348.

(16) Liu, X.; Webb, T.; Dai, L.; Ji, K.; Smith, J. A.; Kilbride, R. C.; Yavari, M.; Bi, J.; Ren, A.; Huang, Y.; Wang, Z.; Shen, Y.; Shao, G.; Sweeney, S. J.; Hinder, S.; Li, H.; Lidzey, D. G.; Stranks, S. D.; Greenham, N. C.; Silva, S. R. P.; Zhang, W. Influence of Halide Choice on Formation of Low-Dimensional Perovskite Interlayer in Efficient Perovskite Solar Cells. *ENERGY Environ. Mater.* **2022**, *5* (2), 670–682.

(17) Sutanto, A. A.; Caprioglio, P.; Drigo, N.; Hofstetter, Y. J.; Garcia-Benito, I.; Quelo, V. I. E.; Neher, D.; Nazeeruddin, M. K.; Stolterfoht, M.; Vaynzof, Y.; Grancini, G. 2D/3D Perovskite Engineering Eliminates Interfacial Recombination Losses in Hybrid Perovskite Solar Cells. *Chem.* **2021**, *7* (7), 1903–1916.

(18) Kodalle, T.; Byranvand, M. M.; Goudreau, M.; Das, C.; Roy, R.; Kot, M.; Briesenick, S.; Zohdi, M.; Rai, M.; Tamura, N.; Flege, J. I.; Hempel, W.; Sutter-Fella, C. M.; Saliba, M. An Integrated Deposition and Passivation Strategy for Controlled Crystallization of 2D/3D Halide Perovskite Films. *Adv. Mater.* **2024**, 2309154.

- (19) Sutter-Fella, C. M. The Value of Watching How Materials Grow: A Multimodal Case Study on Halide Perovskites. *Adv. Energy Mater.* **2021**, *11* (17), No. 2003534.
- (20) Du, K.; Tu, Q.; Zhang, X.; Han, Q.; Liu, J.; Zauscher, S.; Mitzi, D. B. Two-Dimensional Lead(II) Halide-Based Hybrid Perovskites Templated by Acene Alkylamines: Crystal Structures, Optical Properties, and Piezoelectricity. *Inorg. Chem.* **2017**, *56* (15), 9291–9302.
- (21) Byun, J.; Cho, H.; Wolf, C.; Jang, M.; Sadhanala, A.; Friend, R. H.; Yang, H.; Lee, T.-W. Efficient Visible Quasi-2D Perovskite Light-Emitting Diodes. *Adv. Mater.* **2016**, *28* (34), 7515–7520.
- (22) Weidman, M. C.; Seitz, M.; Stranks, S. D.; Tisdale, W. A. Highly Tunable Colloidal Perovskite Nanoplatelets through Variable Cation, Metal, and Halide Composition. *ACS Nano* **2016**, *10* (8), 7830–7839.
- (23) Nobuaki Kitazawa, N. K. Optical Absorption and Photoluminescence Properties of Pb(I, Br)-Based Two-Dimensional Layered Perovskite. *Jpn. J. Appl. Phys.* **1997**, *36* (4R), 2272.
- (24) Wright, N. E.; Qin, X.; Xu, J.; Kelly, L. L.; Harvey, S. P.; Toney, M. F.; Blum, V.; Stiff-Roberts, A. D. Influence of Annealing and Composition on the Crystal Structure of Mixed-Halide, Ruddlesden–Popper Perovskites. *Chem. Mater.* **2022**, *34* (7), 3109–3122.
- (25) Yang, S.; Niu, W.; Wang, A.-L.; Fan, Z.; Chen, B.; Tan, C.; Lu, Q.; Zhang, H. Ultrathin Two-Dimensional Organic–Inorganic Hybrid Perovskite Nanosheets with Bright, Tunable Photoluminescence and High Stability. *Angew. Chem., Int. Ed.* **2017**, *56* (15), 4252–4255.
- (26) Hoke, E. T.; Slotcavage, D. J.; Dohner, E. R.; Bowring, A. R.; Karunadasa, H. I.; McGehee, M. D. Reversible Photo-Induced Trap Formation in Mixed-Halide Hybrid Perovskites for Photovoltaics. *Chem. Sci.* **2015**, *6* (1), 613–617.
- (27) Beal, R. E.; Hagström, N. Z.; Barrier, J.; Gold-Parker, A.; Prasanna, R.; Bush, K. A.; Passarello, D.; Schelhas, L. T.; Brüning, K.; Tassone, C. J.; Steinrück, H.-G.; McGehee, M. D.; Toney, M. F.; Nogueira, A. F. Structural Origins of Light-Induced Phase Segregation in Organic–Inorganic Halide Perovskite Photovoltaic Materials. *Matter* **2020**, *2* (1), 207–219.
- (28) Brennan, M. C.; Draguta, S.; Kamat, P. V.; Kuno, M. Light-Induced Anion Phase Segregation in Mixed Halide Perovskites. *ACS Energy Lett.* **2018**, *3* (1), 204–213.
- (29) Limmer, D. T.; Ginsberg, N. S. Photoinduced Phase Separation in the Lead Halides Is a Polaronic Effect. *J. Chem. Phys.* **2020**, *152* (23), No. 230901.
- (30) Bischak, C. G.; Hetherington, C. L.; Wu, H.; Aloni, S.; Ogletree, D. F.; Limmer, D. T.; Ginsberg, N. S. Origin of Reversible Photoinduced Phase Separation in Hybrid Perovskites. *Nano Lett.* **2017**, *17* (2), 1028–1033.
- (31) Philippe, B.; Saliba, M.; Correa-Baena, J.-P.; Cappel, U. B.; Turren-Cruz, S.-H.; Grätzel, M.; Hagfeldt, A.; Rensmo, H. Chemical Distribution of Multiple Cation (Rb⁺, Cs⁺, MA⁺, and FA⁺) Perovskite Materials by Photoelectron Spectroscopy. *Chem. Mater.* **2017**, *29* (8), 3589–3596.
- (32) Kim, G. Y.; Senocrate, A.; Yang, T.-Y.; Gregori, G.; Grätzel, M.; Maier, J. Large Tunable Photoeffect on Ion Conduction in Halide Perovskites and Implications for Photodecomposition. *Nat. Mater.* **2018**, *17* (5), 445–449.
- (33) Boyd, C. C.; Cheacharoen, R.; Leijtens, T.; McGehee, M. D. Understanding Degradation Mechanisms and Improving Stability of Perovskite Photovoltaics. *Chem. Rev.* **2019**, *119* (5), 3418–3451.
- (34) Hu, Y.; Schlipf, J.; Wussler, M.; Petrus, M. L.; Jaegermann, W.; Bein, T.; Müller-Buschbaum, P.; Docampo, P. Hybrid Perovskite/Perovskite Heterojunction Solar Cells. *ACS Nano* **2016**, *10* (6), 5999–6007.
- (35) Rademeyer, M. 2-Phenylethylammonium Bromide. *Acta Crystallogr. Sect. E Struct. Rep. Online* **2007**, *63* (1), o221–o223.
- (36) Proppe, A. H.; Johnston, A.; Teale, S.; Mahata, A.; Quintero-Bermudez, R.; Jung, E. H.; Grater, L.; Cui, T.; Filleter, T.; Kim, C.-Y.; Kelley, S. O.; De Angelis, F.; Sargent, E. H. Multication Perovskite 2D/3D Interfaces Form via Progressive Dimensional Reduction. *Nat. Commun.* **2021**, *12* (1), 3472.
- (37) Chen, M.-Y.; Lin, J.-T.; Hsu, C.-S.; Chang, C.-K.; Chiu, C.-W.; Chen, H. M.; Chou, P.-T. Strongly Coupled Tin-Halide Perovskites to Modulate Light Emission: Tunable 550–640 nm Light Emission (FWHM 36–80 nm) with a Quantum Yield of up to 6.4%. *Adv. Mater.* **2018**, *30* (20), No. 1706592.
- (38) Calabrese, J.; Jones, N. L.; Harlow, R. L.; Herron, N.; Thorn, D. L.; Wang, Y. Preparation and Characterization of Layered Lead Halide Compounds. *J. Am. Chem. Soc.* **1991**, *113* (6), 2328–2330.
- (39) Morrow, D. J.; Hautzinger, M. P.; Lafayette, D. P. I.; Scheeler, J. M.; Dang, L.; Leng, M.; Kohler, D. D.; Wheaton, A. M.; Fu, Y.; Guzei, I. A.; Tang, J.; Jin, S.; Wright, J. C. Disentangling Second Harmonic Generation from Multiphoton Photoluminescence in Halide Perovskites Using Multidimensional Harmonic Generation. *J. Phys. Chem. Lett.* **2020**, *11* (16), 6551–6559.
- (40) Yang, Y.; Peng, X.; Qin, C.; Lian, Y.; Gao, J.; Yang, X. Accelerating Energy Funnel and Charge Transport of Quasi-2D Perovskites for Efficient Sky Blue- and White-Light-Emitting Devices. *ACS Photonics* **2022**, *9* (1), 163–172.
- (41) Ng, Y. F.; Febriansyah, B.; Jamaludin, N. F.; Giovanni, D.; Yantara, N.; Chin, X. Y.; Tay, Y. B.; Sum, T. C.; Mhaisalkar, S.; Mathews, N. Design of 2D Templating Molecules for Mixed-Dimensional Perovskite Light-Emitting Diodes. *Chem. Mater.* **2020**, *32* (19), 8097–8105.
- (42) Yuan, M.; Quan, L. N.; Comin, R.; Walters, G.; Sabatini, R.; Voznyy, O.; Hoogland, S.; Zhao, Y.; Beauregard, E. M.; Kanjanaboos, P.; Lu, Z.; Kim, D. H.; Sargent, E. H. Perovskite Energy Funnels for Efficient Light-Emitting Diodes. *Nat. Nanotechnol.* **2016**, *11* (10), 872–877.
- (43) Jacobsson, T. J.; Correa-Baena, J.-P.; Halvani Anaraki, E.; Philippe, B.; Stranks, S. D.; Bouduban, M. E. F.; Tress, W.; Schenk, K.; Teuscher, J.; Moser, J.-E.; Rensmo, H.; Hagfeldt, A. Unreacted PbI₂ as a Double-Edged Sword for Enhancing the Performance of Perovskite Solar Cells. *J. Am. Chem. Soc.* **2016**, *138* (32), 10331–10343.
- (44) Cappel, U. B.; Svanström, S.; Lanzilotto, V.; Johansson, F. O. L.; Aitola, K.; Philippe, B.; Giangrisostomi, E.; Ovsyannikov, R.; Leitner, T.; Föhlich, A.; Svensson, S.; Mårtensson, N.; Boschloo, G.; Lindblad, A.; Rensmo, H. Partially Reversible Photoinduced Chemical Changes in a Mixed-Ion Perovskite Material for Solar Cells. *ACS Appl. Mater. Interfaces* **2017**, *9* (40), 34970–34978.
- (45) Frost, J. M.; Walsh, A. What Is Moving in Hybrid Halide Perovskite Solar Cells? *Acc. Chem. Res.* **2016**, *49* (3), 528–535.
- (46) Cho, J.; Mathew, P. S.; DuBose, J. T.; Kamat, P. V. Photoinduced Halide Segregation in Ruddlesden–Popper 2D Mixed Halide Perovskite Films. *Adv. Mater.* **2021**, *33* (48), No. 2105585.
- (47) Chakkamalayath, J.; Hiott, N.; Kamat, P. V. How Stable Is the 2D/3D Interface of Metal Halide Perovskite under Light and Heat? *ACS Energy Lett.* **2023**, *8* (1), 169–171.
- (48) Lee, J.-W.; Dai, Z.; Han, T.-H.; Choi, C.; Chang, S.-Y.; Lee, S.-J.; De Marco, N.; Zhao, H.; Sun, P.; Huang, Y.; Yang, Y. 2D Perovskite Stabilized Phase-Pure Formamidinium Perovskite Solar Cells. *Nat. Commun.* **2018**, *9* (1), 3021.
- (49) Zhou, Y.; Herz, L. M.; Jen, A. K.-Y.; Saliba, M. Advances and Challenges in Understanding the Microscopic Structure–Property–Performance Relationship in Perovskite Solar Cells. *Nat. Energy* **2022**, *7* (9), 794–807.
- (50) deQuilettes, D. W.; Yoo, J. J.; Brenes, R.; Kosasih, F. U.; Laitz, M.; Dou, B. D.; Graham, D. J.; Ho, K.; Shi, Y.; Shin, S. S.; Ducati, C.; Bawendi, M. G.; Bulović, V. Reduced Recombination via Tunable Surface Fields in Perovskite Thin Films. *Nat. Energy* **2024**, 457–466.
- (51) McGovern, L.; Koschany, L.; Grimaldi, G.; Muscarella, L. A.; Ehrler, B. Grain Size Influences Activation Energy and Migration Pathways in MAPbBr₃ Perovskite Solar Cells. *J. Phys. Chem. Lett.* **2021**, *12* (9), 2423–2428.
- (52) Shao, Y.; Fang, Y.; Li, T.; Wang, Q.; Dong, Q.; Deng, Y.; Yuan, Y.; Wei, H.; Wang, M.; Gruverman, A.; Shield, J.; Huang, J. Grain Boundary Dominated Ion Migration in Polycrystalline Organic–

Inorganic Halide Perovskite Films. *Energy Environ. Sci.* **2016**, *9* (5), 1752–1759.

(53) Mathew, P. S.; Kamat, P. V. Cation Migration in Physically Paired 2D and 3D Lead Halide Perovskite Films. *Adv. Opt. Mater.* **2024**, *12* (8), No. 2300957.

(54) Szabó, G.; Kamat, P. V. How Cation Migration across a 2D/3D Interface Dictates Perovskite Solar Cell Efficiency. *ACS Energy Lett.* **2024**, *9* (1), 193–200.

(55) Seetharaman, A.; Narra, S.; Rajamanickam, P.; Putikam, R.; Lin, M.-C.; Wei-Guang Diao, E. Diffusion of Bulky Organic Cations in the 3D/2D Heterostructures to Form Interfacial Quasi-2D (N₂) Phase for Tin Perovskite Solar Cells. *J. Mater. Chem. A* **2023**, *11* (39), 21089–21098.

(56) Laurita, G.; Fabini, D. H.; Stoumpos, C. C.; Kanatzidis, M. G.; Seshadri, R. Chemical Tuning of Dynamic Cation Off-Centering in the Cubic Phases of Hybrid Tin and Lead Halide Perovskites. *Chem. Sci.* **2017**, *8* (8), 5628–5635.

(57) Schueller, E. C.; Laurita, G.; Fabini, D. H.; Stoumpos, C. C.; Kanatzidis, M. G.; Seshadri, R. Crystal Structure Evolution and Notable Thermal Expansion in Hybrid Perovskites Formamidinium Tin Iodide and Formamidinium Lead Bromide. *Inorg. Chem.* **2018**, *57* (2), 695–701.

(58) Perini, C. A. R.; Castro-Mendez, A.-F.; Kodalle, T.; Ravello, M.; Hidalgo, J.; Gomez-Dominguez, M.; Li, R.; Taddei, M.; Giridharagopal, R.; Pothoof, J.; Sutter-Fella, C. M.; Ginger, D. S.; Correa-Baena, J.-P. Vapor-Deposited $n = 2$ Ruddlesden–Popper Interface Layers Aid Charge Carrier Extraction in Perovskite Solar Cells. *ACS Energy Lett.* **2023**, *8* (3), 1408–1415.

(59) Guthrey, H.; Moseley, J. A Review and Perspective on Cathodoluminescence Analysis of Halide Perovskites. *Adv. Energy Mater.* **2020**, *10* (26), No. 1903840.

(60) Bischak, C. G.; Sanehira, E. M.; Pecht, J. T.; Luther, J. M.; Ginsberg, N. S. Heterogeneous Charge Carrier Dynamics in Organic–Inorganic Hybrid Materials: Nanoscale Lateral and Depth-Dependent Variation of Recombination Rates in Methylammonium Lead Halide Perovskite Thin Films. *Nano Lett.* **2015**, *15* (7), 4799–4807.

(61) Bischak, C. G.; Wong, A. B.; Lin, E.; Limmer, D. T.; Yang, P.; Ginsberg, N. S. Tunable Polaron Distortions Control the Extent of Halide Demixing in Lead Halide Perovskites. *J. Phys. Chem. Lett.* **2018**, *9* (14), 3998–4005.

(62) Duong, T.; Mulmudi, H. K.; Shen, H.; Wu, Y.; Barugkin, C.; Mayon, Y. O.; Nguyen, H. T.; Macdonald, D.; Peng, J.; Lockrey, M.; Li, W.; Cheng, Y.-B.; White, T. P.; Weber, K.; Catchpole, K. Structural Engineering Using Rubidium Iodide as a Dopant under Excess Lead Iodide Conditions for High Efficiency and Stable Perovskites. *Nano Energy* **2016**, *30*, 330–340.

(63) Zhang, H.; Pfeifer, L.; Zakeeruddin, S. M.; Chu, J.; Grätzel, M. Tailoring Passivators for Highly Efficient and Stable Perovskite Solar Cells. *Nat. Rev. Chem.* **2023**, *7* (9), 632–652.

(64) Zhu, T.; Zheng, D.; Liu, J.; Coolen, L.; Pauporté, T. PEAI-Based Interfacial Layer for High-Efficiency and Stable Solar Cells Based on a MAcl-Mediated Grown FA_{0.94}MA_{0.06}PbI₃ Perovskite. *ACS Appl. Mater. Interfaces* **2020**, *12* (33), 37197–37207.

(65) Mitzi, D. B.; Feild, C. A.; Harrison, W. T. A.; Guloy, A. M. Conducting Tin Halides with a Layered Organic-Based Perovskite Structure. *Nature* **1994**, *369* (6480), 467–469.

(66) Wang, K.; Wu, C.; Yang, D.; Jiang, Y.; Priya, S. Quasi-Two-Dimensional Halide Perovskite Single Crystal Photodetector. *ACS Nano* **2018**, *12* (5), 4919–4929.

(67) Park, S. M.; Wei, M.; Xu, J.; Atapattu, H. R.; Eickemeyer, F. T.; Darabi, K.; Grater, L.; Yang, Y.; Liu, C.; Teale, S.; Chen, B.; Chen, H.; Wang, T.; Zeng, L.; Maxwell, A.; Wang, Z.; Rao, K. R.; Cai, Z.; Zakeeruddin, S. M.; Pham, J. T.; Risko, C. M.; Amassian, A.; Kanatzidis, M. G.; Graham, K. R.; Grätzel, M.; Sargent, E. H. Engineering Ligand Reactivity Enables High-Temperature Operation of Stable Perovskite Solar Cells. *Science* **2023**, *381* (6654), 209–215.

(68) Ahmad, S.; Fu, P.; Yu, S.; Yang, Q.; Liu, X.; Wang, X.; Wang, X.; Guo, X.; Li, C. Dion-Jacobson Phase 2D Layered Perovskites for Solar Cells with Ultrahigh Stability. *Joule* **2019**, *3* (3), 794–806.